ARTICLE OPEN

Check for updates

Coherent propagation of spin-orbit excitons in a correlated metal

Valentin Zimmermann[1], Arvind Kumar Yogi[1,2], Deniz Wong[3], Christian Schulz[3], Maciej Bartkowiak[3], Klaus Habicht[3,4], Lichen Wang[1], Masahiko Isobe[1], Matteo Minola[1], Giniyat Khaliullin[1], Bernhard Keimer[1]✉ and Matthias Hepting[1]✉

Collective excitations such as plasmons and paramagnons are fingerprints of atomic-scale Coulomb and exchange interactions between conduction electrons in metals. The strength and range of these interactions, which are encoded in the excitations' dispersion relations, are of primary interest in research on the origin of collective instabilities such as superconductivity and magnetism in quantum materials. Here we report resonant inelastic x-ray scattering experiments on the correlated 4*d*-electron metal Sr_2RhO_4, which reveal a spin-orbit entangled collective excitation. The dispersion relation of this mode is opposite to those of antiferromagnetic insulators such as Sr_2IrO_4, where the spin-orbit excitons are dressed by magnons. The presence of propagating spin-orbit excitons implies that the spin-orbit coupling in Sr_2RhO_4 is unquenched, and that collective instabilities in 4*d*-electron metals and superconductors must be described in terms of spin-orbit entangled electronic states.

npj Quantum Materials (2023)8:53 ; https://doi.org/10.1038/s41535-023-00585-4

INTRODUCTION

The presence of strong intra-atomic spin-orbit coupling (SOC) in quantum materials can give rise to a variety of many-body phenomena, ranging from spin liquid phases to topologically protected states[1–3]. Since the SOC constant λ scales with the atomic number, it is strong in 5*d*-electron materials, while it is naturally less prominent in 4*d* and 3*d* systems. Nonetheless, it can still shape the electronic and magnetic properties of the latter materials. For instance, SOC is a critical ingredient for the emergence of excitonic magnetism in the 4*d* antiferromagnetic (AFM) Mott insulator Ca_2RuO_4[4–9], and it can lead to prevalent Kitaev exchange interactions in other 4*d* ruthenates[10] as well as in 3*d* cobaltates[11].

Collective excitations (quasiparticles) that possess a spin-orbit-entangled character are hallmarks of the role of SOC in shaping the electronic properties of quantum materials. Notably, the dispersion relation of such spin-orbit exciton (SOE) modes encodes the relevant microscopic interaction parameters, from which model Hamiltonians can be constructed, as demonstrated for several insulating 3*d* materials[12–15]. Another example is the 5*d* AFM Mott insulator Sr_2IrO_4, where strong SOC splits the t_{2g}-orbital manifold into separated bands with total angular momentum $j = 1/2$ and $3/2$[16–22], and a SOE mode arises from transitions of holes across the split manifold[23–28]. Resonant inelastic x-ray scattering (RIXS) experiments at the Ir L_3-edge[23,24] and at the O *K*-edge[26–28] found that the SOE dispersion exhibits a maximum at the Γ-point and a minimum at the AFM Brillouin zone (BZ) boundary. The corresponding propagation of the SOE can be described by theories that include the interaction with magnons in the exciton hopping process[23,24]. In hole- and electron-doped Sr_2IrO_4 without long-range AFM order, the SOE retains its typical dispersion as long as short-lived magnetic excitations (paramagnons) exist[29,30].

Recently, the influence of the intra-atomic SOC on the electronic structure and macroscopic properties of correlated metals has moved into the center of attention. For instance, the debate about the role of SOC for the unconventional superconductivity in the correlated 4*d* metal Sr_2RuO_4[31–36] has been revived[37–40]. Yet, whereas collective excitations of conduction electrons in metallic systems, such as plasmons[41,42] and paramagnons[43,44], have been extensively studied, the propagation of spin-orbit entangled modes in such systems has remained elusive. One notable exception are heavy-fermion metals[45] where spin-orbit excitations can be mediated by the Ruderman-Kittel-Kasuya-Yosida (RKKY) interaction between local *f*-electron moments and conduction electrons[46], which, however, is quite different from Sr_2RuO_4 where only *d*-electrons are situated at the Fermi level.

Here we use RIXS at the O *K*-edge to examine the low-energy excitation spectrum of the correlated 4*d*-electron material Sr_2RhO_4. Similarly to Sr_2RuO_4, the material is a paramagnetic (PM) metal with a sharply defined Fermi surface[47–49], but with one additional valence electron its $4d^5$ configuration is isoelectronic to Sr_2IrO_4 ($5d^5$). The distinct insulating AFM ground state of the latter material is usually rationalized by its narrow, half-filled $j = 1/2$ band that is further split into upper and lower Hubbard bands due to on-site Coulomb repulsion U[16,17]. In the case of Sr_2RhO_4, it was suggested that the moderate SOC is incapable of fully splitting the $j = 1/2$ and $3/2$ bands, and thus even an increased U cannot open a Mott gap, leaving the material metallic[17]. Specifically, extensive studies on the electronic structure of Sr_2RhO_4 pointed out that the metallic ground state is actually the result of a concerted interplay between SOC, Coulomb interaction, and structural distortions[49–52], although the definite role of SOC and whether it acts in an effective, 'Coulomb-enhanced'[53,54] fashion is still under debate. Most importantly, however, it is not clear to what extent the ionic $j = 1/2$ and $3/2$ picture, which is natural for insulating materials, is applicable in a correlated metal.

Our RIXS experiment reveals a well-defined, dispersive SOE mode, whose emergence is an explicit manifestation of the splitting of the t_{2g} manifold into bands carrying total angular

[1]Max Planck Institute for Solid State Research, Heisenbergstraße 1, D-70569 Stuttgart, Germany. [2]UGC-DAE Consortium for Scientific Research (CSR), Indore Centre, University Campus, Khandwa Road, Indore, (M.P.) 452001, India. [3]Helmholtz-Zentrum Berlin für Materialien und Energie, Hahn-Meitner-Platz 1, D-14109 Berlin, Germany. [4]Institute of Physics and Astronomy, University of Potsdam, Karl-Liebknecht-Straße 24/25, D-14476 Potsdam, Germany. ✉email: b.keimer@fkf.mpg.de; hepting@fkf.mpg.de

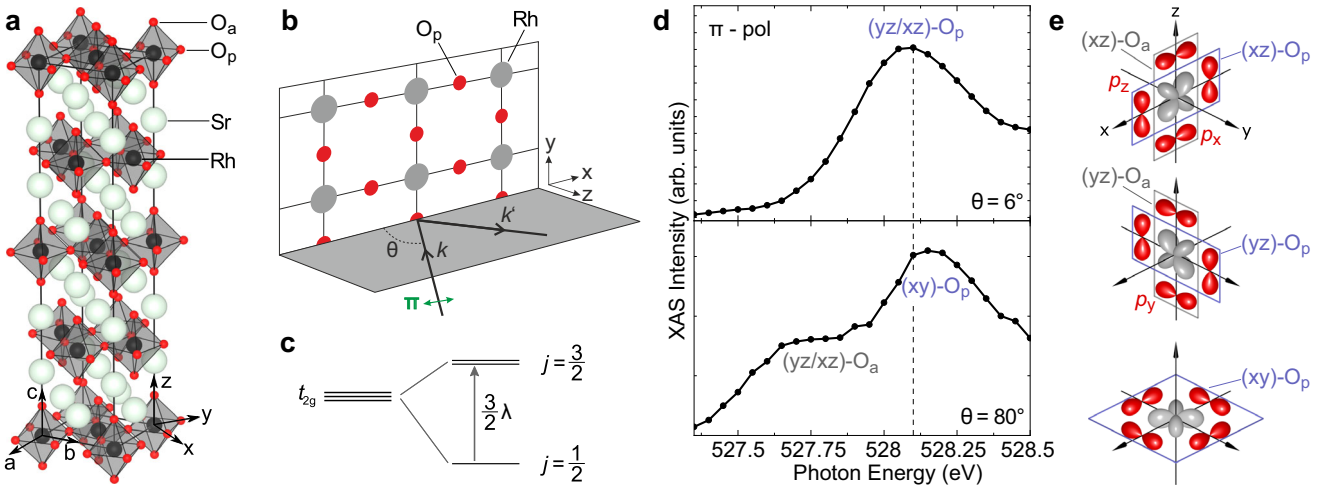

Fig. 1 Experimental scattering geometry and orbital states probed in XAS and RIXS. a Crystal structure of Sr_2RhO_4, with the solid black lines corresponding to the tetragonal unit cell. The crystallographic *a*, *b*, and *c*-axis are indicated, as well the *x*, *y*, and *z*-axis of the RhO_6 octahedral reference frame. The labels O_a and O_p mark the apical and in-plane oxygen ions, respectively. **b** Schematic of the scattering geometry of the O *K*-edge RIXS experiment. The square planar lattice of a RhO_2 plane is illustrated, where the RhO_6 octahedral tilts are omitted for simplicity. The scattering plane (gray) is spanned by the *z*-direction and either the *x*- or the diagonal $x + y$ direction (not shown here). The former case corresponds to transfer of the projected in-plane momentum along the (0,0)-(π,0) direction in reciprocal space, and the latter case along the (0,0)-(π,π) direction. The incident photons are linearly π-polarized, and **k** (***k'***) corresponds to the incoming (outgoing) photon beam. The angle between **k** and the sample surface is denoted by θ. **c** Splitting of the t_{2g} hole level into the $j = 1/2$ and 3/2 spin-orbit multiplets. **d** XAS across the O *K*-edge measured in total electron yield for $\theta = 6°$ (top panel) and $\theta = 80°$ (bottom panel). The vertical dashed line marks the incident photon energy (528.1 eV) used for the RIXS measurements. The labels refer to the Rh t_{2g} orbitals (d_{xz}, d_{yz}, d_{xy}) that are hybridized with 2*p* states either from the O_a or O_p ions. **e** Schematics of the orbital hybridizations that are relevant in **d**. Blue (gray) boxes indicate hybridizations with in-plane (apical) oxygen *p* orbitals.

momentum $j = 1/2$ and 3/2, in close analogy to the spin-orbit split electronic structure of Sr_2IrO_4. We observe, however, that the SOE in Sr_2RhO_4 exhibits a markedly distinct dispersion relation, which we model and discuss in the context of the different ground states of the two materials. Our results provide insights into the collective dynamics of spin-orbit entangled quasiparticles, which had previously remained elusive in correlated metallic systems.

RESULTS

Identification of orbital states in XAS

The experiment was performed on Sr_2RhO_4 single-crystals grown by the optical floating zone method (see Materials and Methods). Figure 1a shows the unit cell of Sr_2RhO_4 in the tetragonal space group $I4_1/acd$, which is closely related to Sr_2IrO_4[55]. The lattice parameters $a, b = 5.45$ Å and $c = 25.75$ Å were determined from a Rietveld refinement of powder x-ray diffraction data of a pulverized Sr_2RhO_4 crystal (see Supplementary Note 1). The scattering geometry used for the XAS and RIXS measurements is sketched in Fig. 1b. While the scattering angle between the incoming (**k**) and outgoing photon beam (***k'***) was fixed to 130°, the projected momentum transfer within the RhO_2 planes could be varied by changing the incident angle θ. Furthermore, an azimuthal rotation of the sample by 45° (not shown here) allowed us to orient the in-plane momentum transfer either along the Rh-O-Rh bond direction [(0,0)-(π,0) direction], or along the diagonal direction [(0,0)-(π,π) direction]. Note that the former direction coincides (approximately) with the *x*/*y* direction as defined within the RhO_6 octahedral network (Fig. 1a), while the latter direction coincides with the crystallographic *a*/*b* direction.

Figure 1d shows the XAS pre-edge structure of the O *K*-edge of Sr_2RhO_4, which corresponds to transitions into unoccupied states of hybridized O 2*p* and Rh 4*d* (t_{2g}) orbitals. Clear differences are visible between spectra taken for θ close to grazing incidence (upper panel) and close to normal incidence (lower panel). The angular dependence of the XAS features is due to the spatial extensions of the lobes of the three active Rh t_{2g}-orbitals (d_{xz}, d_{yz}, d_{xy}), as well as crystallographically distinct oxygen sites of the RhO_6 octahedra, differentiating the apical (O_a) and the in-plane oxygen sites (O_p). Depending on the chosen scattering geometry, the XAS signal contains contributions from specific combinations of the Rh t_{2g} orbitals with either the O_a or the O_p ions, each of which possesses three different *p* orbitals (p_x, p_y, p_z). Schematics of the Rh-O hybridized orbital states that are relevant for our study are displayed in Fig. 1e. The assignment of the XAS features in Fig. 1d to these hybridized states is consistent with a previous O *K*-edge XAS study on Sr_2RhO_4[56].

Spin-orbit entangled excitations in RIXS

Figure 2 shows RIXS spectra measured with an incident photon energy of 528.1 eV. For small θ, this energy coincides with the XAS resonance energy of Rh d_{yz} and d_{xz} states hybridized with p_z orbitals of the planar O_p ions (Fig. 1d). For larger values of θ, the Rh d_{xy} states hybridized with p_x and p_y orbitals of O_p become the dominant feature in the XAS (Fig. 1d), although we note that the maximum of the latter XAS resonance is situated at slightly higher energies. A comprehensive survey of the dependence of the inelastic features in the RIXS spectra as a function of the incident energy and the incident angle θ is given in Supplementary Fig. 3. Notably, we find that the low-energy features in the RIXS spectra (below 1 eV energy loss), on which we will focus in the following, do not depend significantly on the incident energy. In fact, the peak around 300 meV energy loss in Fig. 2 is present across the entire Rh d_{yz}/d_{xz} resonance for $\theta = 6°$, as well as the d_{xy} resonance for $\theta = 80°$, although the peak intensity decreases when moving away from the XAS maximum energy (see Supplementary Fig. 3). However, the~300 meV peak is absent (or below the detection limit) when the incident photon energy is tuned to 527.6 eV, which corresponds to the resonance of the Rh d_{yz}/d_{xz} states hybridized with p_y/p_x orbitals of the O_a ions (Fig. 1d and Supplementary Fig. 3). As a consequence of these observations, the

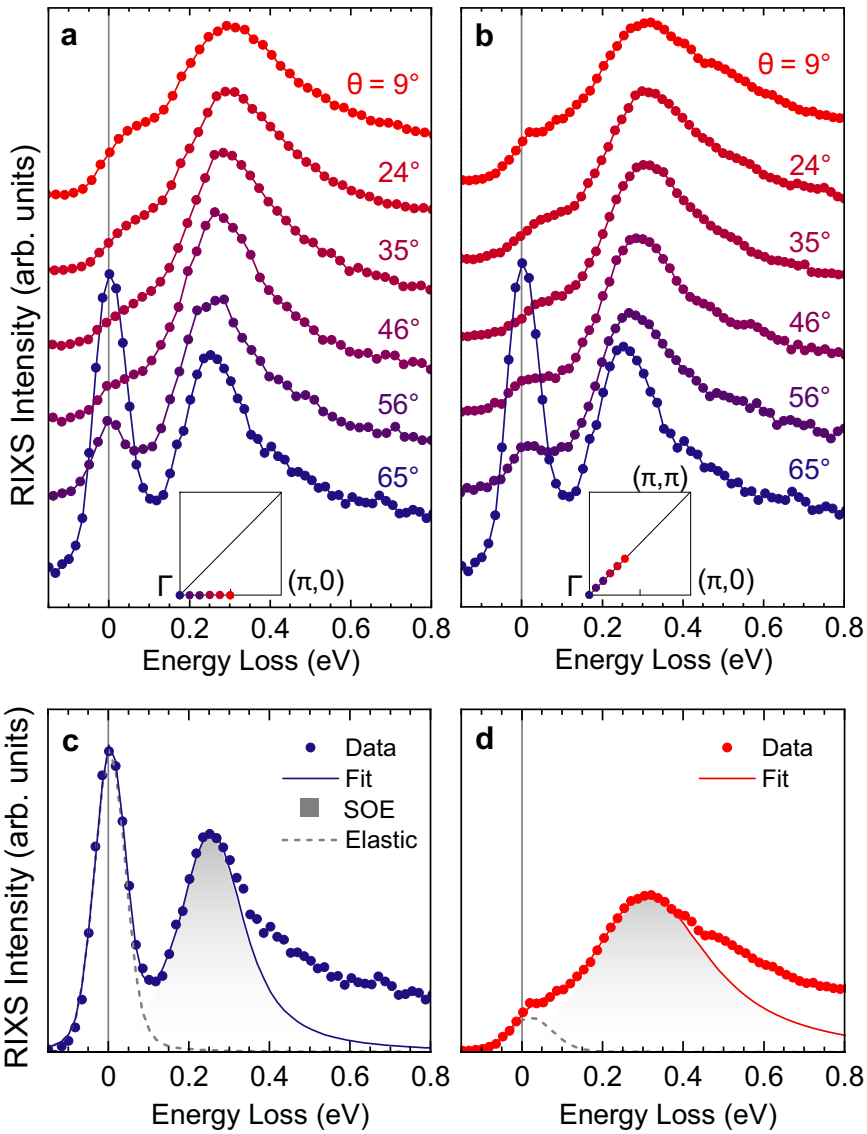

Fig. 2 Spin-orbit exciton in Sr_2RhO_4. O *K*-edge RIXS spectra taken at different incident angles θ, which varies the projected in-plane momentum transfer along (**a**), the (0,0)-(π,0) direction and (**b**), the (0,0)-(π,π) direction, as illustrated in the insets. Spectra are offset in vertical direction for clarity. **c** Exemplary fit (solid blue line) of the RIXS spectrum taken at $\theta = 65°$. The fitted peak profiles of the quasi-elastic line (gray dotted line) and the SOE (gray area) are indicated. **d** Exemplary fit (solid red line) of the RIXS spectrum taken at $\theta = 9°$ for the (0,0)-(π,π) direction.

key RIXS measurements of this study (Fig. 2) were carried out exclusively at 528.1 eV.

As a first step, we inspect the RIXS spectra in Fig. 2a. Each spectrum in the panel was collected at a different in-plane momentum transfer, which was achieved by varying the incident angle θ. The corresponding coverage of the in-plane BZ along the (0,0)-(π,0) direction is illustrated in the inset in Fig. 2a. As the central result, we find that the peak centered around ~300 meV for $\theta = 65°$ disperses to higher energies for increasing momentum transfer (decreasing θ), and broadens in its linewidth. A similar behavior is observed when the momentum transfer is oriented along the (0,0)-(π,π) direction (Fig. 2b). For a detailed analysis, we fit the RIXS spectra by the sum of the quasi-elastic peak situated around zero-energy loss and a damped harmonic oscillator (DHO) function[57] that accounts for the dispersive peak around ~300 meV. Two exemplary fit results are shown in Fig. 2c, d, while the complete set of fitted spectra and additional information about the fitting procedure are given in the Methods section and Supplementary Fig. 4. Note that the DHO model is used due to the broad linewidth and asymmetric lineshape of the peak, which is present even at (0,0) momentum transfer, i.e., at the 2D BZ center. The application of the DHO model is further justified when considering it is strongly damped, in particular for large momentum transfers where the damping parameter extracted in the fits becomes comparable to ω_0 (Fig. 3a, b). Nevertheless, while the DHO fit captures the rising edge of the dispersive peak accurately (Fig. 2c, d), a single DHO function does not account for additional spectral weight that emerges at higher energy losses. This spectral weight is essentially featureless and reminiscent of a broad background contribution, which will be discussed in more detail below.

The oscillator frequencies ω_0 extracted with the DHO model are shown in Fig. 3a (filled blue symbols). In addition, we display the positions of the maximum spectral intensity (open blue symbols) for comparison. Both positions are similar in proximity to the BZ

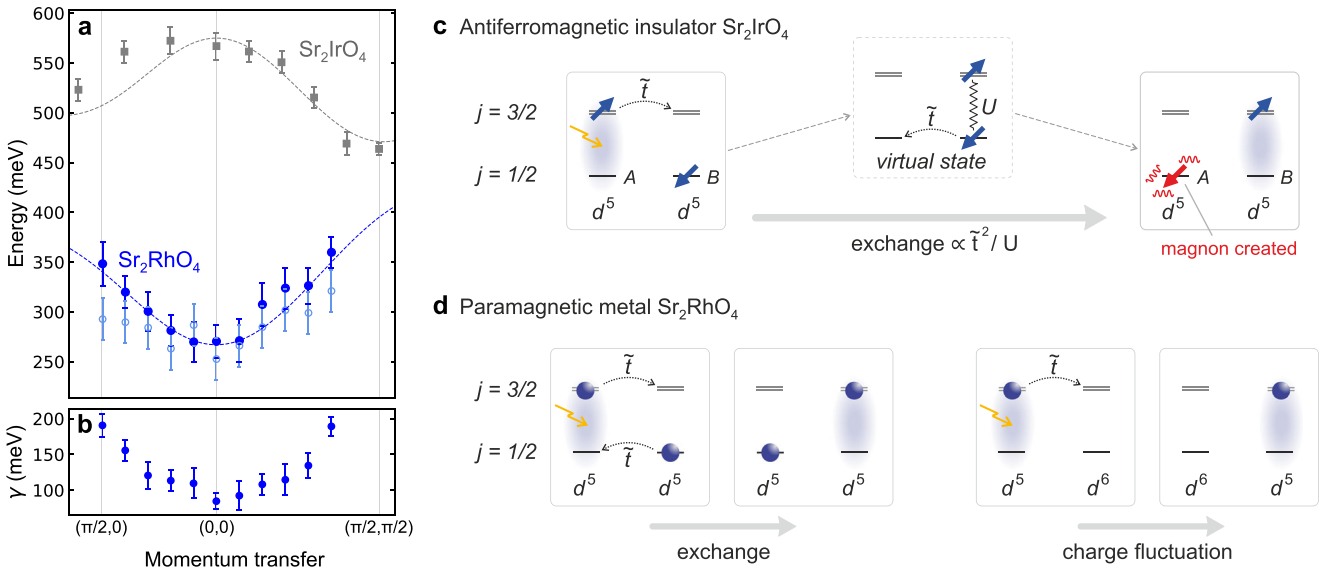

Fig. 3 Exciton dispersion and propagation in Sr_2RhO_4 and Sr_2IrO_4. a Energy ω_0 of the SOE (filled blue symbols) extracted from fits of the RIXS spectra with a DHO model (see text and Fig. 2) plotted as a function of the in-plane momentum transfer in units of $1/a'$, where $a' = a/\sqrt{2}$ is the Rh-Rh bond length. The positions of the maximum spectral intensity (open blue symbols) are superimposed for comparison. Filled gray symbols correspond to the energy of the SOE in Sr_2IrO_4, extracted by Lorentzian fits of Ir L_3-edge RIXS data in ref. [24]. The gray (blue) line corresponds to a tight-binding model for the exciton hopping in Sr_2IrO_4 (Sr_2RhO_4). **b** Damping parameter γ from the DHO fits. The procedure for determining the error bars is detailed in the Methods sections. **c** Schematic of the incoherent nearest-neighbor hopping of the SOE in an AFM background. We use the hole language which is convenient to describe the d^5 configuration containing a single hole in the t_{2g} manifold. Lattice site A (B) represents spin-up (spin-down) magnetic sublattice of the Ir-d^5 ions. The orange arrow indicates the promotion of A site from the $j = 1/2$ ground state (black spin) to the excited $j = 3/2$ state (blue spin). The blue cloud represents the exciton. Hole hopping between neighboring sites is denoted by $\tilde{t}$. In the virtual state, holes interact via the on-site Coulomb repulsion U. In the final state of the exchange process, the resulting occupation (red spin) of the A site is incompatible with the magnetic order of the sublattices (red wiggled lines) and a magnon is created. As a consequence, exciton hopping from A to B is incoherent. An additional hopping of the exciton to a next-nearest neighbor (not shown here) can create another frustrated spin that is required for a double-spin flip to reestablish the proper sublattice order. **d** Coherent hopping of the SOE in a paramagnetic metal. A t_{2g} hole in the ground (excited) state of d^5 ion is indicated by blue sphere. Left: the exchange process involving high-energy ($\propto U$) virtual states as in Sr_2IrO_4 but without a magnon creation. Right: the exciton motion in Sr_2RhO_4 using a single hole hopping between Rh ions with different charge configurations, d^5 and d^6, which are present in the metallic ground state. Charge fluctuations between d^5 and d^4 states (discussed in Supplementary Note 4) similarly contribute to the exciton hopping.

center at (0,0), but deviate for large momentum transfer along the (0,0)-(π,0) and (0,0)-(π,π) directions. This deviation arises because for large damping of the DHO, the center of the peak no longer coincides with the actual oscillator frequency ω_0. Since the damping parameter γ in the DHO fits becomes larger for higher momentum transfers (Fig. 3b), the discrepancy between dispersion and peak position thus increases towards the zone boundary. Because the DHO model has the spectral correspondence of a collective mode, whereas the direct physical meaning of maximum spectral intensity might be ambiguous, we focus on the ω_0 positions in the following.

In any case, we note that the two differently extracted peak energies both fall into an energy interval between ≈250 and 375 meV, with the minimum energy at (0,0). This energy scale is significantly higher than the reported single- and bimagnon energies in Sr_2IrO_4, which revolve around 40 meV[58] and 160 meV[26], respectively. Typical magnon energies in 4*d*-electron compounds are also well below 100 meV[3,5–7]. We therefore rule out a purely magnetic origin of the dispersive Sr_2RhO_4 peak. Furthermore, we consider its assignment to a peak seen in optical conductivity[59] as implausible, because this peak is centered only around 180 meV and reproduced by theoretical calculations both with and without SOC[54]. Optical transitions that involve $p-d$ charge transfer were reported at energies higher than 2 eV[56] and can also be observed in our RIXS spectra at these high energies (Supplementary Fig. 3). On the other hand, the energy regime of our observed low-energy peak is remarkably similar to $\frac{3}{2}\lambda \approx 285$ meV, that is, the energy difference between the $j = 1/2$ and 3/2 levels in the t_{2g} manifold (Fig. 1c), according to the free-ion SOC constant $\lambda \approx 190$ meV of Rh^{4+}[60]. Moreover, quantum chemistry calculations predict a spin-orbit excitation around 250 meV in Sr_2RhO_4[61]. In analogy to Sr_2IrO_4, we therefore assign the observed mode to excitations of a hole across the spin-orbit split t_{2g} manifold, which is referred to as SOE[23,24].

Comparison to excitons in iridates

A direct comparison between the SOE dispersions in Sr_2RhO_4 and Sr_2IrO_4 is provided in Fig. 3a. The most distinctive differences are that the energy scale in Sr_2IrO_4 is higher and the curvature of the dispersion curves around the Γ-point (0,0) is inverted. We note that the SOE energy in Sr_2IrO_4 was determined from fits with Lorentzian functions to Ir L_3-edge RIXS data in ref. [24]. While the differences in the data analysis and RIXS process possibly obscure details for a quantitative comparison of the two compounds, the statements about the different energy scales and curvature of the dispersions are robust.

In the 5*d* material Sr_2IrO_4, the expected SOC splitting is large, $\frac{3}{2}\lambda \approx 570$ meV[24], which explains the distinct energy scales in Fig. 3a. Notably, for Sr_2RhO_4, the good agreement between the observed SOE energy and $\frac{3}{2}\lambda$ indicates that SOC is neither quenched nor 'Coulomb-enhanced'. We note, however, that a decisive determination of the mode energy requires future RIXS experiments with the improved resolution or the use of complementary techniques, such as Raman spectroscopy[25].

The inverted dispersions in Fig. 3a imply that the exciton propagation processes in the AFM insulator and nonmagnetic metal are qualitatively different. In Sr_2IrO_4, exciton motion involves the exchange of the $j = 1/2$ and $j = 3/2$ states, using high-energy virtual hoppings of electrons between Ir^{4+} ions (Fig. 3c), similar to spin-exchange in magnets. In the AFM state, the nearest-neighbor exciton hopping creates a flipped spin, i.e., a magnon, and a coherent motion of the exciton is only possible within the same (A or B) magnetic sublattice[23,24], when the pairs of flipped spins can relax into the AFM ground state. This results in a dispersion minimum at the AFM zone boundary $(\frac{\pi}{2},\frac{\pi}{2})$ and a maximum at the Γ-point[24], in close analogy to the motion of a doped hole in the AFM CuO_2 planes of cuprates[62].

In paramagnetic Sr_2RhO_4, the exciton hopping does not generate magnons, and no band-folding effects, associated with the magnetic unit cell doubling, occur. The major difference from Sr_2IrO_4 is, however, that the metallic ground state of Sr_2RhO_4 comprises valence states other than the dominant $Rh^{4+}(d^5)$ one, in particular $Rh^{3+}(d^6)$ and $Rh^{5+}(d^4)$. Charge fluctuations between these states can promote the SOE motion without involving any high-energy exchange processes (Fig. 3d, right panel). The overall amplitude of this contribution is proportional to the densities of the d^6 and d^4 charge configurations, and its sign is given by the sign of the hopping integral of the t_{2g} electrons. The latter is negative, because this hopping is mainly via the oxygen p orbitals[53], i.e., $t = -t_{pd}^2/\Delta_{pd}$, where t_{pd} is the overlap between Rh and O states and $\Delta_{pd} > 0$ is the charge-transfer gap. Therefore, the SOE dispersion is determined by two competing mechanisms: a virtual exchange process that dominates in the Mott insulator Sr_2IrO_4, and a real charge transfer process that generates the dispersion minimum at the Γ-point in metallic Sr_2RhO_4.

On a qualitative level, the SOE hopping amplitude is $\tau \sim 2\tilde{t}^2/U - 2\tilde{t}n$, where n is the average density of the d^6 charge states (which is equal to that of the d^4 states), reduced from its 'free-electron' value by the on-site Coulomb repulsion. The parameter $\tilde{t} \simeq \frac{2}{3}t_{pd}^2/\Delta_{pd}$ refers to the hoppings between the spin-orbit j levels in Fig. 3 and includes the SOC projection factor of 2/3. A quantitative theory should include mixing of the SOE modes with the underlying electronic particle-hole continuum, as the exciton motion in metals is coupled to the fermionic density fluctuations (Fig. 3d). The observed broad linewidth of the SOE and the additional spectral weight that is not captured by the DHO fits (Fig. 2c, d and Methods) might be a signature of this mixing.

Modeling of the exciton propagation

Further insights into the dispersion of the SOE can be gleaned from the application of a semi-quantitative tight-binding model on a square lattice, representing the Rh (Ir) sites in the RhO_2 (IrO_2) planes, with τ_1, τ_2, and τ_3, the nearest, next-nearest, and third-nearest neighbor exciton hopping parameters, respectively. In a model capturing the dispersion of Sr_2IrO_4, the hopping amplitudes are positive, with τ_1 possessing a small value, while τ_2 and τ_3 are large and of similar magnitude. The small value of τ_1 is due to the AFM background, which inhibits a coherent nearest-neighbor hopping[23,24] (Fig. 3c). The resulting dispersion for a parameter choice with a $\tau_1:\tau_2:\tau_3$ ratio of 1:4:4 and $\tau_1 = 2$ meV is shown as the gray line in Fig. 3a.

In contrast, the hopping amplitudes for Sr_2RhO_4 are negative, and the τ_1 value is dominant, for instance such that the $\tau_1:\tau_2:\tau_3$ ratio is 4:1:0.7 and $\tau_1 = -20$ meV (blue line in Fig. 3a). The leading τ_1 value is rationalized by a coherent hopping of SOE in the PM background, as shown in Fig. 3d, and its negative value implies a predominance of the second term in the relation $\tau \sim 2\tilde{t}^2/U - 2\tilde{t}n$ introduced above. In fact, with $t_{pd}^2/\Delta_{pd} \approx 0.2$ eV typical for t_{2g} electrons, the Coulomb interaction $U \approx 2.3$ eV in Sr_2RhO_4[54], and a density $n \approx 1/8$, this estimate yields a τ_1 comparable to the one obtained from our modeling. It is interesting to note that in terms of the Hubbard model, the above value of n places Sr_2RhO_4 halfway between the free-electron and the Mott-insulating limits ($n = 1/4$ and $n = 0$, correspondingly).

Despite the significantly smaller values of τ_2 and τ_3 compared to τ_1 in Sr_2RhO_4, a model that completely disregards them fails to describe the experimentally observed dispersion around (0,0) well. We interpret the necessity to include τ_2 and τ_3 as a consequence of the spatially extended character of the 4d wavefunctions, which may result in longer-range hoppings. Nevertheless, for the precise determination of the $\tau_1:\tau_2:\tau_3$ ratio, data of the SOE energies beyond the maximum momentum transfer of the present O K-edge RIXS experiment would be required. Future experiments that provide a wider coverage of reciprocal space, for instance Rh L_3-edge RIXS or inelastic neutron scattering, are therefore highly desirable.

DISCUSSION

In summary, our observation and description of a collective, spin-orbit entangled mode provide direct evidence for the significance of SOC in Sr_2RhO_4. The presence of the mode indicates that the splitting of the t_{2g} manifold into states with total angular momentum $j = 1/2$ and 3/2 is an essential ingredient of the low-energy electronic structure of Sr_2RhO_4, which needs to be taken into account in future theoretical models of this material and other 4d-electron compounds. We find that the energy scale of the SOE mode is close to 3/2 of the SOC constant λ of Rh^{4+}, which implies the presence of unquenched orbital moments. Our comparison to the SOE dispersion in the AFM insulating 5d analogue Sr_2IrO_4 reveals how excitonic quasiparticles behave when they propagate on a metallic background and magnonic dressings are stripped off.

Furthermore, our results suggest that the SOE is a property of the RhO_2 planes and possesses a 2D-like character, as the mode resonates exclusively at energies that correspond to hybridized states of Rh and planar O sites (Supplementary Fig. 3). Such a character is reminiscent of the extensively studied excitons in 2D layered materials, including monolayer transition metal dichalcogenides[63]. Notably, the propagation of excitons in the latter materials can be controlled by external tuning parameters[64], and a bosonic condensation can be achieved for instance by optical pumping[65]. Whether the properties of the SOE in Sr_2RhO_4 can be tuned in a similar fashion remains to be examined in future studies.

Extending our findings beyond Sr_2RhO_4, our insights into the differences of the SOE propagation in antiferromagnetic insulating versus metallic systems hold significant implications for a variety of 4d and 5d transition metal compounds, including those based on ruthenium[8,66–72]. In particular, the charge fluctuation mechanism might also be critical for the SOE propagation in the correlated metal and superconductor Sr_2RuO_4, where previous RIXS experiments at the O K-edge have reported a spin-orbit entangled mode with an energy of a few hundred meV[67] and a study at the Ru L_3-edge has identified dispersive branches of spin-orbital excitations[73]. Yet, the d^4 ground state of the Ru^{4+} ions with two holes in the t_{2g} shell suggests the emergence of a more complex SOE multiplet structure than that of Rh and Ir ions in d^5 configuration, calling for complementary experimental and theoretical investigations.

METHODS

Sample growth

Single crystals of Sr_2RhO_4 were synthesized using the optical-floating zone technique. Off-stoichiometric quantities of Rh_2O_3 (Alfa Aesar, 99.9%) and $SrCO_3$ (Alfa Aesar, 99.994%) powder with the molar ratio 1.15:4 were ground together and calcinated at 1100 °C for 36 hrs. Subsequently the powder was reground and compressed into a dense rod which was then sintered at 1400 °C

for 48 hrs. To promote the oxidization of Rh^{3+} to Rh^{4+}, both calcination steps were performed under flowing O_2 gas. The floating zone growth was performed using a CSC FZ-T-10000-H-II-VP furnace equipped with four 1.5 kW halogen lamps. A maximum of 7 bar oxygen partial gas pressure was applied and crystals were grown at a rate of 10 mm/hr to limit the amount of evaporation from highly volatile Rh-oxides. The largest single-crystals had dimensions of approximately 1.5 cm × 0.5 cm × 0.4 cm, and it was found that the crystals cleave easily. A characterization of the physical properties of the crystals is given in the Supplementary Note 1.

RIXS experiment

The XAS and RIXS spectra were collected at the U41-PEAXIS beamline[74–76] of BESSY II at the HZB, Berlin. The measurements were carried out at $T = 15$ K with linearly π-polarized photons with energies tuned to the O K-edge (≈530 eV). The effective energy resolution of the RIXS measurements was $\Delta E \approx 90$ meV. The scattering geometry of the experiment is sketched in Fig. 1b.

Analysis of the RIXS data

An overview of all fitted RIXS spectra is presented in Supplementary Fig. 4. The zero-energy loss in each spectrum was determined by acquiring a reference spectrum from carbon-tape prior to each measurement at different incident angles. To that end, a thin piece of carbon tape film which covers a small portion of the sample surface was attached on the Sr_2RhO_4 single-crystal. The effect of height difference between sample and tape was found to be negligible by scanning the tape at multiple positions along the beam. The employed energy resolution did not allow us to resolve fine details around zero-energy loss. Therefore, the elastic peak was modeled by a Voigt function[77,78], capturing both elastic and quasi-elastic contributions in a single peak. The SOE was modeled using a damped harmonic oscillator (DHO) function[57], which can be expressed as

$$f(\omega) \propto \frac{\gamma\omega}{\left(\omega^2 - \omega_0^2\right)^2 + 4\gamma^2\omega^2,} \quad (1)$$

where ω_0 denotes the oscillator frequency and γ is the damping parameter. The experimental energy resolution of $\Delta E = 90$ meV was taken into account via Gaussian convolution of the DHO function. Note that for large damping, the oscillator frequency can deviate from the position ω_p of the peak maximum, as $\omega_0^2 = \omega_p^2 + \gamma^2$ (for $\gamma \leq \omega_0$). As a consequence, we find that the peak position and ω_0 deviate in the RIXS spectra in Figs. 2 and 3 for high momentum transfers, where the SOE feature becomes increasingly broad due to larger damping[79]. An additional complication arises from excess spectral weight at the high-energy shoulder of the SOE peak, which cannot be captured by the DHO function employed for the SOE. The emergence of this spectral weight can be due to the particle-hole continuum or multiple-exciton processes, and is reminiscent of the asymmetry of the SOE feature in the O K-edge RIXS spectra of Sr_2IrO_4[26,27]. In our approach, we do not attempt to capture this incoherent contribution by fitting additional peaks at higher energies. Instead, we only fit the 'coherent' part of the peak, that is, the low-energy shoulder as well as a small range of the high-energy shoulder. A possible error that can be introduced by the choice of the cut-off of the fitting range of the high-energy shoulder is reflected by the error bars for ω_0 shown in Fig. 3a. Specifically, we extracted ω_0 for a number of different fits with differently chosen cut-offs of the fitting range of the high-energy shoulder (see Supplementary Fig. 5). The resulting spread of ω_0 is indicated by the error bars at the filled blue symbols in Fig. 3a. The average energy defines the position of the data point. The error bars of open blue symbols in Fig. 3a reflect a conservative estimate of the uncertainty in our assignment of the maximum of the intensity, in correspondence to the sampling interval of our RIXS data points, which is 16 meV.

DATA AVAILABILITY

The data that support the findings of this study are available from the corresponding author upon reasonable request.

CODE AVAILABILITY

The numerical codes used to generate the results in this work are available from the corresponding authors on reasonable request.

Received: 22 February 2023; Accepted: 26 September 2023;
Published online: 05 October 2023

REFERENCES

1. Witczak-Krempa, W., Chen, G., Kim, Y. B. & Balents, L. Correlated quantum phenomena in the strong spin-orbit regime. *Annu. Rev. Condens. Matter Phys.* **5**, 57–82 (2014).
2. Rau, J. G., Lee, E. K.-H. & Kee, H.-Y. Spin-Orbit Physics Giving Rise to Novel Phases in Correlated Systems: Iridates and Related Materials. *Annu. Rev. Condens. Matter Phys.* **7**, 195–221 (2016).
3. Takayama, T., Chaloupka, J., Smerald, A., Khaliullin, G. & Takagi, H. Spin-Orbit-Entangled Electronic Phases in 4*d* and 5*d* Transition-Metal Compounds. *J. Phys. Soc. Jpn.* **90**, 062001 (2021).
4. Khaliullin, G. Excitonic Magnetism in Van Vleck–type d^4 Mott Insulators. *Phys. Rev. Lett.* **111**, 197201 (2013).
5. Kunkemöller, S. et al. Highly Anisotropic Magnon Dispersion in Ca_2RuO_4: Evidence for Strong Spin Orbit Coupling. *Phys. Rev. Lett.* **115**, 247201 (2015).
6. Jain, A. et al. Higgs mode and its decay in a two-dimensional antiferromagnet. *Nat. Phys.* **13**, 633–637 (2017).
7. Souliou, S.-M. et al. Raman Scattering from Higgs Mode Oscillations in the Two-Dimensional Antiferromagnet Ca_2RuO_4. *Phys. Rev. Lett.* **119**, 067201 (2017).
8. Gretarsson, H. et al. Observation of spin-orbit excitations and Hund's multiplets in Ca_2RuO_4. *Phys. Rev. B* **100**, 045123 (2019).
9. Feldmaier, T., Strobel, P., Schmid, M., Hansmann, P. & Daghofer, M. Excitonic magnetism at the intersection of spin-orbit coupling and crystal-field splitting. *Phys. Rev. Res.* **2**, 033201 (2020).
10. Takagi, H., Takayama, T., Jackeli, G., Khaliullin, G. & Nagler, S. E. Concept and realization of Kitaev quantum spin liquids. *Nat. Rev. Phys.* **1**, 264–280 (2019).
11. Liu, H., Chaloupka, J. & Khaliullin, G. Kitaev Spin Liquid in 3*d* Transition Metal Compounds. *Phys. Rev. Lett.* **125**, 047201 (2020).
12. Buyers, W. J. L., Holden, T. M., Svensson, E. C., Cowley, R. A. & Hutchings, M. T. Excitations in $KCoF_3$. II. Theoretical. *J. Phys. C: Solid State Phys.* **4**, 2139–2159 (1971).
13. Schlappa, J. et al. Spin-orbital separation in the quasi-one-dimensional Mott insulator Sr_2CuO_3. *Nature* **485**, 82–85 (2012).
14. Sarte, P. M. et al. Spin-orbit excitons in CoO. *Phys. Rev. B* **100**, 075143 (2019).
15. Yuan, B. et al. Spin-orbit exciton in a honeycomb lattice magnet $CoTiO_3$: revealing a link between magnetism in *d*- and *f*-electron systems. *Phys. Rev. B* **102**, 134404 (2020).
16. Bertinshaw, J., Kim, Y., Khaliullin, G. & Kim, B. Square Lattice Iridates. *Annu. Rev. Condens. Matter Phys.* **10**, 315–336 (2019).
17. Kim, B. J. et al. Novel $J_{\rm eff} = 1/2$ Mott State Induced by Relativistic Spin-Orbit Coupling in Sr_2IrO_4. *Phys. Rev. Lett.* **101**, 076402 (2008).
18. Moon, S. J. et al. Dimensionality-Controlled Insulator-Metal Transition and Correlated Metallic State in 5*d* Transition Metal Oxides $Sr_{n+1}Ir_nO_{3n+1}$ ($n = 1, 2$, and ∞). *Phys. Rev. Lett.* **101**, 226402 (2008).
19. Jackeli, G. & Khaliullin, G. Mott Insulators in the Strong Spin-Orbit Coupling Limit: From Heisenberg to a Quantum Compass and Kitaev Models. *Phys. Rev. Lett.* **102**, 017205 (2009).
20. Kim, B. J. et al. Phase-Sensitive Observation of a Spin-Orbital Mott State in Sr_2IrO_4. *Science* **323**, 1329–1332 (2009).
21. Watanabe, H., Shirakawa, T. & Yunoki, S. Microscopic Study of a Spin-Orbit-Induced Mott Insulator in Ir Oxides. *Phys. Rev. Lett.* **105**, 216410 (2010).
22. Zwartsenberg, B. et al. Spin-orbit-controlled metal-insulator transition in Sr_2IrO_4. *Nat. Phys.* **16**, 290–294 (2020).
23. Kim, J. et al. Magnetic Excitation Spectra of Sr_2IrO_4 Probed by Resonant Inelastic X-Ray Scattering: Establishing Links to Cuprate Superconductors. *Phys. Rev. Lett.* **108**, 177003 (2012).

24. Kim, J. et al. Excitonic quasiparticles in a spin-orbit Mott insulator. *Nat. Commun.* **5**, 4453 (2014).
25. Yang, J.-A. et al. High-energy electronic excitations in Sr_2IrO_4 observed by Raman scattering. *Phys. Rev. B* **91**, 195140 (2015).
26. Lu, X. et al. Dispersive magnetic and electronic excitations in iridate perovskites probed by oxygen *K*-edge resonant inelastic x-ray scattering. *Phys. Rev. B* **97**, 041102 (2018).
27. Ilakovac, V. et al. Oxygen states in La- and Rh-doped Sr_2IrO_4 probed by angle-resolved photoemission and O *K*-edge resonant inelastic x-ray scattering. *Phys. Rev. B* **99**, 035149 (2019).
28. Paris, E. et al. Strain engineering of the charge and spin-orbital interactions in Sr_2IrO_4. *Proc. Natl Acad. Sci. USA* **117**, 24764–24770 (2020).
29. Gretarsson, H. et al. Persistent paramagnons deep in the metallic phase of $Sr_{2-x}La_xIrO_4$. *Phys. Rev. Lett.* **117**, 107001 (2016).
30. Clancy, J. P. et al. Magnetic excitations in hole-doped Sr_2IrO_4: comparison with electron-doped cuprates. *Phys. Rev. B* **100**, 104414 (2019).
31. Ng, K. K. & Sigrist, M. The role of spin-orbit coupling for the superconducting state in Sr_2RuO_4. *EPL* **49**, 473–479 (2000).
32. Yanase, Y., Takamatsu, S. & Udagawa, M. Spin-orbit coupling and multiple phases in spin-triplet superconductor Sr_2RuO_4. *J. Phys. Soc. Jpn.* **83**, 061019 (2014).
33. Ramires, A. & Sigrist, M. Identifying detrimental effects for multiorbital superconductivity: application to Sr_2RuO_4. *Phys. Rev. B* **94**, 104501 (2016).
34. Cobo, S., Ahn, F., Eremin, I. & Akbari, A. Anisotropic spin fluctuations in Sr_2RuO_4: role of spin-orbit coupling and induced strain. *Phys. Rev. B* **94**, 224507 (2016).
35. Kim, B., Khmelevskyi, S., Mazin, I. I., Agterberg, D. F. & Franchini, C. Anisotropy of magnetic interactions and symmetry of the order parameter in unconventional superconductor Sr_2RuO_4. *npj Quantum Mater.* **2**, 37 (2017).
36. Kim, M., Mravlje, J., Ferrero, M., Parcollet, O. & Georges, A. Spin-orbit coupling and electronic correlations in Sr_2RuO_4. *Phys. Rev. Lett.* **120**, 126401 (2018).
37. Suh, H. G. et al. Stabilizing even-parity chiral superconductivity in Sr_2RuO_4. *Phys. Rev. Res.* **2**, 032023 (2020).
38. Petsch, A. N. et al. Reduction of the Spin Susceptibility in the Superconducting State of Sr_2RuO_4 Observed by Polarized Neutron Scattering. *Phys. Rev. Lett.* **125**, 217004 (2020).
39. Clepkens, J., Lindquist, A. W. & Kee, H.-Y. Shadowed triplet pairings in Hund's metals with spin-orbit coupling. *Phys. Rev. Res.* **3**, 013001 (2021).
40. Gingras, O., Allaglo, N., Nourafkan, R., Côté, M. & Tremblay, A.-M. S. Superconductivity in correlated multiorbital systems with spin-orbit coupling: Coexistence of even- and odd-frequency pairing, and the case of Sr_2RuO_4. *Phys. Rev. B* **106**, 064513 (2022).
41. Hill, J. P., Kao, C.-C., Caliebe, W. A. C., Gibbs, D. & Hastings, J. B. Inelastic X-Ray Scattering Study of Solid and Liquid Li and Na. *Phys. Rev. Lett.* **77**, 3665–3668 (1996).
42. Hepting, M. et al. Three-dimensional collective charge excitations in electron-doped copper oxide superconductors. *Nature* **563**, 374–378 (2018).
43. Doubble, R. et al. Direct Observation of Paramagnons in Palladium. *Phys. Rev. Lett.* **105**, 027207 (2010).
44. Le Tacon, M. et al. Intense paramagnon excitations in a large family of high-temperature superconductors. *Nat. Phys.* **7**, 725–730 (2011).
45. Nemkovski, K. S. et al. Polarized-Neutron Study of Spin Dynamics in the Kondo Insulator YbB_{12}. *Phys. Rev. Lett.* **99**, 137204 (2007).
46. Jang, H. et al. Intense low-energy ferromagnetic fluctuations in the antiferromagnetic heavy-fermion metal CeB_6. *Nat. Mater.* **13**, 682–687 (2014).
47. Perry, R. S. et al. Sr_2RhO_4: a new, clean correlated electron metal. *N. J. Phys.* **8**, 175–175 (2006).
48. Baumberger, F. et al. Fermi Surface and Quasiparticle Excitations of Sr_2RhO_4. *Phys. Rev. Lett.* **96**, 246402 (2006).
49. Battisti, I. et al. Direct comparison of ARPES, STM, and quantum oscillation data for band structure determination in Sr_2RhO_4. *npj Quantum Mater.* **5**, 91 (2020).
50. Kim, B. J. et al. Missing *xy*-Band Fermi Surface in 4*d* Transition-Metal Oxide Sr_2RhO_4: Effect of the Octahedra Rotation on the Electronic Structure. *Phys. Rev. Lett.* **97**, 106401 (2006).
51. Haverkort, M. W., Elfimov, I. S., Tjeng, L. H., Sawatzky, G. A. & Damascelli, A. Strong Spin-Orbit Coupling Effects on the Fermi Surface of Sr_2RuO_4 and Sr_2RhO_4. *Phys. Rev. Lett.* **101**, 026406 (2008).
52. Martins, C., Aichhorn, M., Vaugier, L. & Biermann, S. Reduced Effective Spin-Orbital Degeneracy and Spin-Orbital Ordering in Paramagnetic Transition-Metal Oxides: Sr_2IrO_4 versus Sr_2RhO_4. *Phys. Rev. Lett.* **107**, 266404 (2011).
53. Liu, G.-Q., Antonov, V. N., Jepsen, O. & Andersen, O. K. Coulomb-Enhanced Spin-Orbit Splitting: The Missing Piece in the Sr_2RhO_4 Puzzle. *Phys. Rev. Lett.* **101**, 026408 (2008).
54. Zhang, G. & Pavarini, E. Optical conductivity, Fermi surface, and spin-orbit coupling effects in Sr_2RhO_4. *Phys. Rev. B* **99**, 125102 (2019).
55. Crawford, M. K. et al. Structural and magnetic studies of Sr_2IrO_4. *Phys. Rev. B* **49**, 9198–9201 (1994).
56. Moon, S. J. et al. Electronic structures of layered perovskite Sr_2MO_4 (M = Ru, Rh, and Ir). *Phys. Rev. B* **74**, 113104 (2006).
57. Peng, Y. Y. et al. Dispersion, damping, and intensity of spin excitations in the monolayer $(Bi,Pb)_2(Sr,La)_2CuO_{6+\delta}$ cuprate superconductor family. *Phys. Rev. B* **98**, 144507 (2018).
58. Liu, X. et al. Probing single magnon excitations in Sr_2IrO_4 using O *K*-edge resonant inelastic x-ray scattering. *J. Phys. Condens. Matter* **27**, 202202 (2015).
59. Sandilands, L. J. et al. Spin-orbit coupling and interband transitions in the optical conductivity of Sr_2RhO_4. *Phys. Rev. Lett.* **119**, 267402 (2017).
60. Abragam, A. & Bleaney, B.*Electron Paramagnetic Resonance of Transition Ions* (Clarendon Press, Oxford, 1970).
61. Katukuri, V. M. et al. Electronic structure of low-dimensional $4d^5$ oxides: interplay of ligand distortions, overall lattice anisotropy, and spin-orbit interactions. *Inorg. Chem.* **53**, 4833–4839 (2014).
62. Kane, C. L., Lee, P. A. & Read, N. Motion of a single hole in a quantum antiferromagnet. *Phys. Rev. B* **39**, 6880–6897 (1989).
63. Kolobov, A. V. & Tominaga, J.*Two-Dimensional Transition-Metal Dichalcogenides* (Springer Nature, Switzerland, 2016).
64. Su, J.-J. & MacDonald, A. H. How to make a bilayer exciton condensate flow. *Nat. Phys.* **4**, 799–802 (2008).
65. Anton-Solanas, C. et al. Bosonic condensation of exciton-polaritons in an atomically thin crystal. *Nat. Mater.* **20**, 1233–1239 (2021).
66. Suzuki, H. et al. Proximate ferromagnetic state in the Kitaev model material α-$RuCl_3$. *Nat. Commun.* **12**, 4512 (2021).
67. Fatuzzo, C. G. et al. Spin-orbit-induced orbital excitations in Sr_2RuO_4 and Ca_2RuO_4: a resonant inelastic x-ray scattering study. *Phys. Rev. B* **91**, 155104 (2015).
68. Das, L. et al. Spin-orbital excitations in Ca_2RuO_4 revealed by resonant inelastic X-Ray scattering. *Phys. Rev. X* **8**, 011048 (2018).
69. von Arx, K. et al. Resonant inelastic x-ray scattering study of $Ca_3Ru_2O_7$. *Phys. Rev. B* **102**, 235104 (2020).
70. Lebert, B. W. et al. Resonant inelastic x-ray scattering study of α-$RuCl_3$: a progress report. *J. Phys. Condens. Matter* **32**, 144001 (2020).
71. Occhialini, C. A. et al. Local electronic structure of rutile RuO_2. *Phys. Rev. Res.* **3**, 033214 (2021).
72. Lee, J.-H. et al. Multiple spin-orbit excitons in α-$RuCl_3$ from bulk to atomically thin layers. *npj Quantum Mater.* **6**, 43 (2021).
73. Suzuki, H. et al. Distinct spin and orbital dynamics in Sr_2RuO_4. arxiv:2212.00245 (2022).
74. Lieutenant, K. et al. Numerical optimization of a RIXS spectrometer using ray-tracing simulations. *J. Phys. Condens. Matter* **738**, 012104 (2016).
75. Lieutenant, K. et al. Design concept of the high-resolution end-station PEAXIS at BESSY II: Wide-Q-range RIXS and XPS measurements on solids, solutions, and interfaces. *J. Electron Spectros. Relat. Phenom.* **210**, 54–65 (2016).
76. Schulz, C. et al. Characterization of the soft X-ray spectrometer PEAXIS at BESSY II. *J. Synchrotron Radiat.* **27**, 238–249 (2020).
77. Takahashi, H. et al. Nonmagnetic $J = 0$ State and Spin-Orbit Excitations in K_2RuCl_6. *Phys. Rev. Lett.* **127**, 227201 (2021).
78. Gretarsson, H. et al. Magnetic excitation spectrum of Na_2IrO_3 probed with resonant inelastic x-ray scattering. *Phys. Rev. B* **87**, 220407 (2013).
79. Lamsal, J. & Montfrooij, W. Extracting paramagnon excitations from resonant inelastic x-ray scattering experiments. *Phys. Rev. B* **93**, 214513 (2016).

ACKNOWLEDGEMENTS

We acknowledge valuable discussions with P. Puphal and V. M. Katukuri. We thank C. Stefani from the X-ray Diffraction Scientific Facility at MPI-FKF for the powder x-ray diffraction measurements and S. Hammoud from the Chemical Synthesis Service Facility at MPI-IS for the ICP-AES measurements. The research was undertaken thanks in part to funding from the Max Planck-UBC-UTokyo Center for Quantum Materials. L. Wang acknowledges support by the Alexander von Humboldt foundation.

AUTHOR CONTRIBUTIONS

M.H., G.K. and B.K. conceived and initiated the project. V.Z. and A.K.Y. synthesized and characterized the samples under the supervision of M.I. The RIXS experiments were carried out by V.Z., D.W., C.S. and M.B. under the supervision of K.H. The data was analyzed and modeled by V.Z., M.H., L.W., M.M. and G.K. The manuscript was written by V.Z., G.K. and M.H., with input from all authors.

FUNDING

Open Access funding enabled and organized by Projekt DEAL.

COMPETING INTERESTS

The authors declare no competing interests.

ADDITIONAL INFORMATION

Supplementary information The online version contains supplementary material available at https://doi.org/10.1038/s41535-023-00585-4.

Correspondence and requests for materials should be addressed to Bernhard Keimer or Matthias Hepting.

Reprints and permission information is available at http://www.nature.com/reprints

Publisher's note Springer Nature remains neutral with regard to jurisdictional claims in published maps and institutional affiliations.